International Journal of Heat and Mass Transfer 52 (2009) 2678–2689

Contents lists available at ScienceDirect

International Journal of Heat and Mass Transfer

journal homepage: www.elsevier.com/locate/ijhmt

Simulation and experimental investigation of pressure loss and heat transfer in microchannel networks containing bends and T-junctions

Daniel Haller [a,*], Peter Woias [a], Norbert Kockmann [b]

[a] Laboratory for Design of Microsystems, Department of Microsystems Engineering (IMTEK), Albert-Ludwigs-University Freiburg, Georges-Köhler-Allee 102, 79110 Freiburg, Germany
[b] Lonza Ltd., Valais works, R&D Exclusive Synthesis, CH-3930 Visp, Switzerland

ARTICLE INFO

Article history:
Received 25 January 2008
Received in revised form 3 September 2008
Available online 21 February 2009

Keywords:
Enhanced heat transfer
Pressure loss
Bent microchannels
Liquid cooling

ABSTRACT

In this paper, the pressure loss and heat transfer in bending and branching microchannels for Re numbers ranging from 10 to 3000 are investigated. Redirecting and splitting the fluid leads to an enhanced heat transfer, but at the same time the pressure loss is increased. The shape of the investigated bends and branchings has a significant influence on both, pressure loss and heat transfer. Fluid flow and heat transfer are simulated for single elements like L-bends and T-joints with different shapes. Test structures are fabricated in silicon and experimentally investigated. The aim of this work is to get an impression of the physical behavior in small elements that enable the development of new liquid cooling systems with higher cooling ability and higher effectiveness.

1. Introduction

With the increasing heat production of electronic devices, the air cooling technology reaches its limits, whereas liquid cooling represents a promising opportunity to develop cooling devices with much higher heat transfer coefficients [1]. In the last years, microreactors have entered the market more and more. These special devices do also need enhanced cooling devices. Therefore, liquid cooling has become a more relevant topic in research, especially cooling systems using microchannels. Current liquid cooling systems use straight microchannels with laminar flow, where the diffusive transport of heat is dominating. Using bent microchannels increases the heat transfer significantly. There are only few publications that investigate the fluid flow behavior of disturbed laminar flow in bent microchannels and even fewer publications regarding the heat transfer in bent microchannels. The pure laminar flow in straight channels is basically understood, see e.g. Gad-el-Hak [2]. The bending and branching disturbs the developed laminar flow. Even though vortices are created through the redirection of the fluid, the flow cannot be treated as turbulent flow, it still is considered as laminar flow. Kockmann et al. [3,4] investigated the fluid flow behavior in bent microchannels. These earlier publications had the main purpose to describe the mixing behavior in bent microchannels, but the created vortices at the bends, that enhance the mixing, enhance the heat transfer as well. This phenomenon is examined in more detail by Kockmann et al. in more recent publications [5,6]. The created vortices guide the cold center flow toward the hot walls and mix colder areas of the fluid with warmer areas, which lead to an enhanced heat transfer. Simple simulations have shown, that a straight channel (L = 1500 μm, w = 100 μm, H = 100 μm, T_{in} = 300 K, T_w = 350 K) absorbs 0.74 W at a Re number of 200, whereas the same channel with a 90° bend after 500 μm absorbs 1.1 W. The cost for the enhanced heat transfer is a higher pressure loss (98 mbar instead of 61 mbar).

Rosaguti et al. [7,8] investigate the heat transfer and pressure drop in periodic, sinusoidal channels with a squared cross-section. In these works not only the enhancement in heat transfer is described, but also the increase in pressure loss. In a straight channel with laminar flow the pressure loss can be calculated using the so called Darcy friction factor. This geometrical factor has been determined for various cross sections and can be used for microchannels, as well (see for example in the work of Papautsky et al. [9]). There are no established scientific methods so far, to approximate the pressure loss caused by a bend and the resulting vortices for laminar flow. For turbulent flow, the pressure loss caused by a bend can be approximated. In this work, different approaches are tested that approximate the overall pressure loss for the flow regime between pure laminar and turbulent flow.

After single, simple elements are characterized and optimized regarding their heat transfer and pressure loss, they can be combined to complex structures with a high heat transfer rate. These complex structures, called fractal structures, are examined in several different research groups. The first one to bring up this idea was Bejan [10,11], which he called "Constructal method". The single elements follow Murray's law, a mathematical description for branching channels, obtained from biological examples like veins in leafs or vessels in the human lung. This law provides a constant

* Corresponding author. Tel.: +49 761 203 7497; fax: +49 761 203 7492.
E-mail address: hallerd@imtek.de (D. Haller).

0017-9310/$ - see front matter © 2009 Elsevier Ltd. All rights reserved.
doi:10.1016/j.ijheatmasstransfer.2008.09.042

Nomenclature

A	channel area (mm^2)
C_f	geometrical wall friction factor (–)
c_p	heat capacity (J kg^{-1} K^{-1})
d_h	hydraulic diameter (μm)
f	Darcy friction factor (–)
h	mean heat transfer coefficient (kW m^{-2} K^{-1})
h_{exp}	experimental heat transfer coefficient (kW m^{-2} K^{-1})
H	channel height (μm)
k	thermal conductivity (W m^{-1} K^{-1})
L	channel length (μm)
$\dot{m}$	mass flow rate (kg h^{-1})
$Nu = d_h h/k$	Nusselt number (–)
Δp	pressure loss (mbar)
$\dot{Q}$	heat flow rate (W)
R_{th}	thermal resistance (K m^2 W^{-1})
$Re = d_h u/v$	Reynolds number (–)
ΔT	temperature difference (K)
u	velocity (m s^{-1})
$\dot{W}$	pumping power (W)
w	channel width (μm)

Greek symbols

η	dynamic viscosity (kg m^{-1} s^{-1})
v	kinetic viscosity (m^2 s^{-1})
ρ	density (kg m^{-3})
ζ_b	bending friction factor (–)

Subscripts

b	bend
exp	experimental
fr	wall friction
H	hotplate
in	inlet
loc	local
log	logarithmic
m	mean
out	outlet
th	thermal
W	wall

wall shear stress throughout the channel network. The influence of Murray's law on pressure loss, flow resistance and wall shear stress in non circular channel networks is examined by Emerson et al. [12]. Zimparov et al. use the "Constructal method" to design a theoretical model of a heat exchanger with a tree-shaped channel network [13]. The same idea was adopted by Chen and Cheng [14]. In this model the flow is assumed to be laminar and fully developed at each location and, therefore, the Nu number remains constant at each location. The influence of vortices on heat transfer is not considered. In a further work Chen and Cheng fabricated a first, very simple device that shows the enhancement in heat transfer of the fractal structure [15]. In the work of Pence [16], the influence of the bending and branching is implemented in the theoretical model and the thermal heat transfer coefficient and thus, the Nu number is changing along the channel. This model clearly shows the higher heat transfer rate at the branchings and in the subsequent microchannels. Detailed numerical simulations of tree-like channel networks from Senn and Poulikakos [17] examine the local pressure loss and heat transfer along channel bifurcations and show the enhancement in heat transfer and pressure loss of channel networks compared to serpentine flow pattern. Their work also confirms the conclusion that the assumption of fully developed flow in channel networks only holds for very low Re numbers.

This work investigates the physical behavior in small elements and networks theoretically with simulations and experimentally with fabricated test structures. After the examined geometries and test structures are introduced, the pressure loss and fluid flow behavior inside these elements is described. The influence of different shapes of bends is shown and mathematical approximations for the pressure loss are developed. In the next step, the heat transfer into the devices and the resulting heat transfer coefficients are described. The last part of this work evaluates the different geometries and test structures regarding the combination of heat transfer and pressure loss. This combined evaluation describes the real effectiveness of the different geometries and test structures.

2. Simulated elements

With the help of the simulation tool CFDACE + 2006 from ESI Group an impression of the physical action inside the cooling channel is obtained. The influence of the shape of the bends and joints is examined regarding heat transfer and pressure loss. The simulated elements are:

1. L-bend: a channel with one 90° bend at constant width.
2. T-joint: a channel that branches into two channels, whose width is reduced by the factor $\sqrt[3]{2}$, according to Murray's law [10].
3. fork-shaped element: a combined element of one T-joint and one following L-bend at each side.

Fig. 1 shows the three different simulated elements in the two different possible versions. Each element can be designed in the first version with 90° bends (Fig. 1a) or 90° joints (Fig. 1b). These

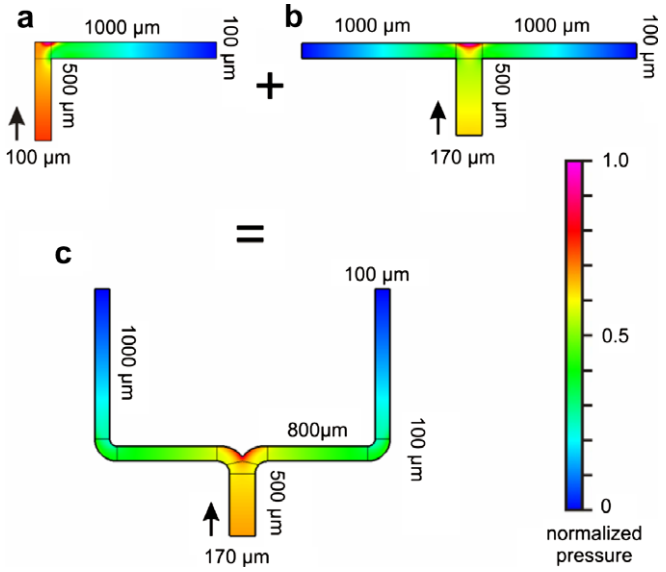

Fig. 1. Different simulated elements with normalized pressure distribution with Re = 200 at inlet: (a) L-bend (90°, heat transfer optimized); (b) T-joint (90°, heat transfer optimized); and (c) fork-shaped element (wedge/radius, pressure optimized).

90° design have a high pressure loss, which can be reduced by replacing the 90° bends by a radius or adding a wedge at the back wall of the T-joint (Fig. 1c). This leads to the second possible version of each element. The radius of the center line is always equal to the channel width. The geometrical data of the simulated elements are included in Fig. 1. The height of each channel is 100 μm. The aim is now, to find a shape that enhances the heat transfer and, at the same time, keeps the pressure loss as low as possible. Different mathematical approaches are tested to find a suitable analytical expression that approximates the pressure loss due to redirection of the fluid. With the knowledge of the simulations, test structures with bending and branching microchannels are fabricated in silicon using standard micromachining tools. These chips enable an investigation of the fundamentals in heat transfer and fluid flow that will help to design more complex devices.

3. Design and fabrication of test structures

There are six different chips that have been designed (see Table 1). All chips have a size of 2×2 cm^2 and are fabricated in silicon. The first design contains a straight channel (SC) and a four times bent channel (L, Fig. 2a). The width of these two channels is 600 μm, the height of the channels of all devices is 300 μm. One version is designed with four 90° bends (L-90), the second version is designed with a radius of the center line of 600 μm at each bend (L-WR). The other designs are more complex and consist of one fork-shaped branch with three branching levels, each. Branches like these are combined in a further work to design a complete cooling device. The first branch is wider (Fig. 2b, FT-W, total width of 14.97 mm) than the other branch (Fig. 2c, FT-N, total width of 11.27 mm), but the respective widths of the channels are all equal. At each T-joint the width is reduced by the factor $\sqrt[3]{2}$, following Murray's law of branching blood vessels [10]. This law provides a constant wall shear stress before and after the branch [18]. With a starting width of 600 μm, the resulting widths after the branching are 337, 217, and 150 μm. Again, there are two versions of each branch. One version consists of 90° bends and joints (-90), the other version contains bends with a radius and joints with a wedge on the backside (-WR). For the same mass flow rate, the versions FT-W-90 and FT-N-90 cause a higher pressure loss with stronger vortices, compared to the respective versions FT-W-WR and FT-N-WR. Therefore, the versions -90 have a higher heat transfer rate and are denoted as heat transfer optimized versions. The versions -WR are denoted as pressure optimized versions.

The chips are fabricated in silicon with standard micromachining tools. Fig. 3 shows the process flow of the fabrication. The silicon wafer is covered with a thermal oxide and a photo resist. The resist is structured and exposed using a printed photomask and UV-light. The structure is transferred into the silicon using the Deep Reactive Ion Etching method (DRIE), a mixed physical and chemical etching method that allows deep, perpendicular walls. Finally, the wafer is covered with a Pyrex wafer and diced into chips. This allows an optical inspection of the flow and thermally isolates the chip.

4. Experimental setup

For the experimental evaluation of the chips, a fluidic mount is manufactured out of PVC with a silicon sealing. The housing has an opening at the top for the optical inspection of the flow, and an opening at the bottom for the connection with a heat source. In the used experimental setup the heat source is a hotplate and the thermal connector is a 20 mm tall combination of two brass blocks. On top of the upper brass block five Pt100-senors ($2.0 \times 2.0 \times 1.3$ mm) from JUMO are attached, that measure the local chip temperature. These sensors are glued into small cavities in the brass block, using a mixture of heat conductivity paste and heat conductivity glue. The cooling chips are pressed against the brass block with a thin layer of heat conductivity paste in-between. Estimations from the measured results show that the sum of the single contact resistances (hot plate to brass block and brass block to cooling chip) varies between 0.5 and 0.7 K W^{-1}. If the contact between brass block and cooling chip was somewhat disturbed, a distinct reduction in heat absorbance was observed. The conductive thermal resistance of the used brass block is 0.12 K W^{-1}. The sum of the thermal contact and conductive resistance of the setup is almost in the range of the determined thermal resistance of the evaluated cooling chips (1–2 K W^{-1}). Hence, inaccuracies in the thermal setup can influence the measurement results and have to be avoided. The pressure and fluid temperature at the inlet and outlet of the fluidic mount is measured using K-type thermoelements from Reckmann and piezo-resistive pressure sensors from Honeywell. In addition, the mass flow rate is measured. The used pump is a micro gear pump from HNP Mikrosysteme with a maximum flow rate of 4.2 l/h. The output signals of the sensors are measured using the data acquisition board SC 2345 from National Instruments together with the Software LabView.

5. Pressure loss

The pressure loss for laminar flow in a bent channel can be separated in two parts. One part is caused by wall friction, the other part is caused by the bend and the resulting vortices (adopted from [19]).

$$\Delta p = \Delta p_{\mathrm{fr}} + \Delta p_{\mathrm{b}} = f \cdot \frac{\rho}{2} u^2$$
$$f = f_{\mathrm{fr}} \frac{L}{d_h} + \zeta_{\mathrm{b}} = \frac{C_{\mathrm{f}}}{\mathrm{Re}} \frac{L}{d_h} + \zeta_{\mathrm{b}} \quad (1)$$

The first term describes the pressure loss caused by wall friction. The geometrical factor C_{f} depends only on the shape of the channel, the roughness of the channel walls is ignored in this work. The value of the factor C_{f} can be obtained from the literature for various cross sections and aspect ratios (e.g. [2]). The second term in Eq. (1) describes the pressure loss caused by the bend. The bending

Table 1
List of all different designs of fabricated chips.

Denomination	Description	Shape of bends and joints
SC-L-90	Straight channel and four times bent channel	90° Bend
SC-L-WR	Straight channel and four times bent channel	Radius
FT-W-90	Wide fork-shaped channel system with three branching levels	90° Bend/90° joint
FT-W-WR	Wide fork-shaped channel system with three branching levels	Radius/wedge
FT-N-90	Narrow fork-shaped channel system with three branching levels	90° Bend/90° joint
FT-N-WR	Narrow fork-shaped channel system with three branching levels	Radius/wedge

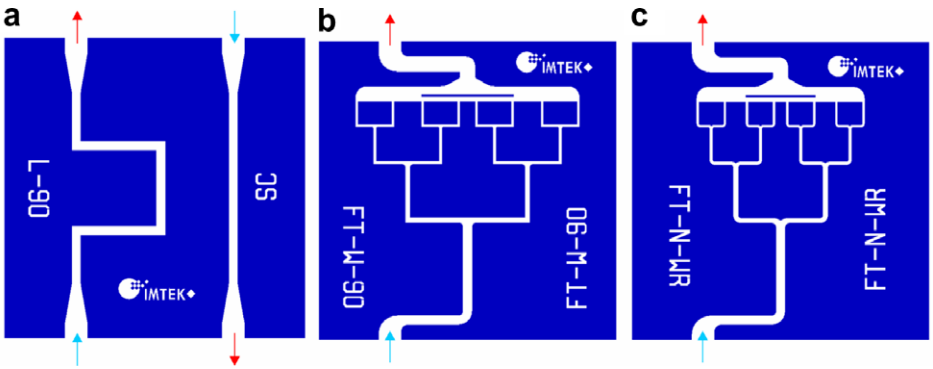

Fig. 2. Mask design of test structures: (a) bent channel L-90 and straight channel SC; (b) FT-W-90: wide branch with 90° bends and joints; and (c) FT-N-WR: narrow branch with wedges and radii.

friction factor ζ_b has been determined for turbulent flow, where ζ_b only depends on the shape of the bend. There have been only few investigations of the bending friction factor for laminar flow, where ζ_b depends on the shape of the bend and the Re number. Replacing the friction factor f of the starting equation by the two separate terms leads to:

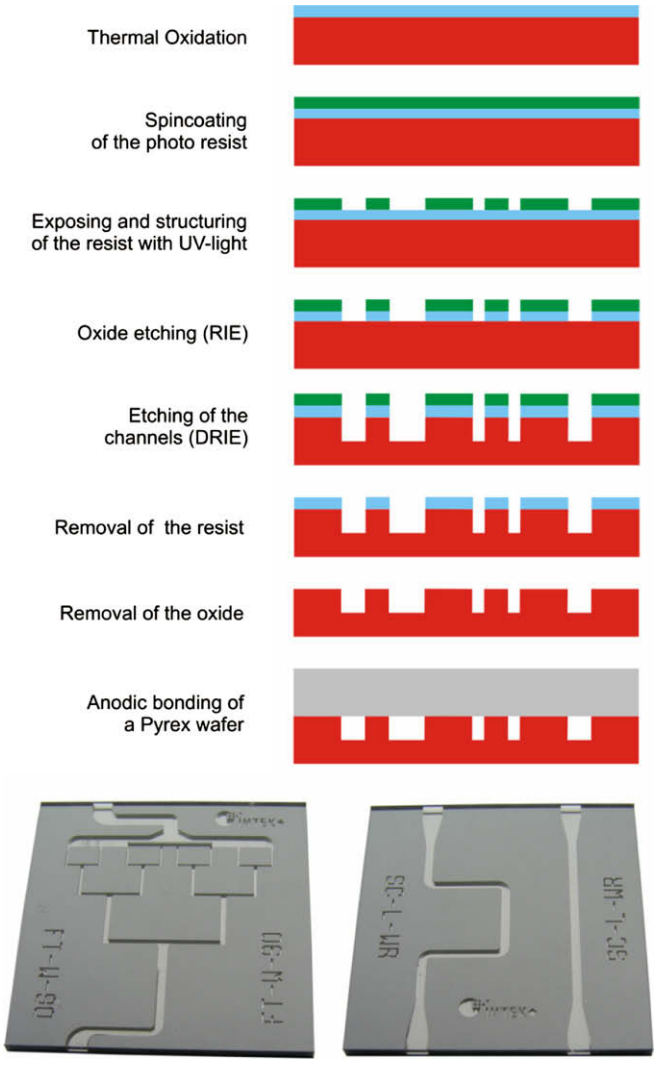

Fig. 3. Process flow of fabrication and examples of fabricated devices.

$$\Delta p = C_f \frac{L}{d_h^2}\frac{\eta}{2}u + \zeta_b \frac{\rho}{2}u^2 \tag{2}$$

For Re numbers lower than 10, the pressure loss caused by wall friction is dominant, the bending friction factor ζ_b is 0. Therefore, the pressure loss is linearly increasing with the flow velocity and the geometrical friction factor C_f can be determined. For higher Re numbers C_f will remain constant and hence, the pressure loss caused by wall friction can be analytically calculated. The difference between overall pressure loss and calculated wall friction pressure loss is the pressure loss caused by the bend. With increasing flow rates the pressure loss caused by the bend becomes more relevant. For Re numbers larger than approximately 2000, the pressure loss caused by the bend and the resulting vortices becomes the dominant part. The wall friction pressure loss is negligible small compared to the bending pressure loss and the bending friction factor ζ_b reaches its asymptotic value of turbulent flow. In the range between these Re numbers, both parts of pressure loss have to be considered.

Starting with the pressure loss within an L-bend or T-joint, see Fig. 5, a fitting equation depending on the velocity or Re number can be used to compare the different shapes of the bend. Using a polynomial equation of second order and the least square regression delivered no useful results. In agreement to Eq. (1), the coefficient of the linear term has to represent the wall friction and should not depend on the shape of the bend of the simulated element. Only the squared term should depend on the shape of the bend. This was not the case, as the bending friction factor also varies with the flow velocity and hence, the pressure loss caused by the bend does not change with the power of 2 with the flow velocity for Re numbers lower than 2000. This makes a polynomial second order equation an unsuitable fitting function. Another possible approach has to be developed. A very simple approach that does not distinguish between wall friction and pressure loss due to the redirection of the fluid, has the form:

$$\Delta p = m\frac{\rho}{2}u^n \tag{3}$$

with the coefficient m and the exponent n, that have to be determined. For turbulent flow the exponent n would be 2 and the coefficient m would be the bending friction factor of the specific geometry. For laminar flow the exponent n lays between 1 and 2, and like the coefficient m, it depends on the geometry. Using a fitting equation with two unknown variables is very difficult, imprecise, and very susceptible to little disturbances in the data. The evaluations of the experimental and simulated results have shown that this approach is not suitable for comparing different geometries and shapes, as well. It can be used for approximating the pressure loss of certain geometry for an arbitrary Re number in the

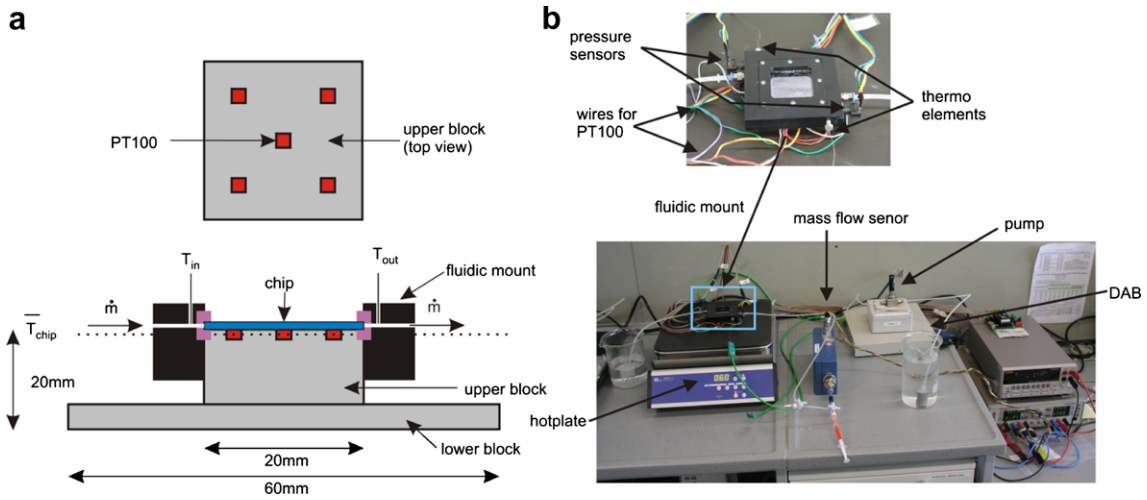

Fig. 4. Experimental setup: (a) schematic setup with both brass blocks, fluidic mount and chip and top view on upper brass block with attached Pt100 (dark squares); and (b) picture of setup and assembled fluidic mount.

examined range, if the pressure loss of several Re numbers for this geometry have been experimentally determined. A more suitable, but also more complex approach has the form:

$$\Delta p = f\frac{L}{d_h}\frac{\rho}{2}u^2 = f^*\frac{L}{d_h}\frac{\rho}{2}\mathrm{Re}^2 \qquad f = m\cdot u^n;\quad f^* = m^*\cdot \mathrm{Re}^n \tag{4}$$

In this approach the Darcy friction factor f is approximated as a function depending on the velocity. For turbulent flow the exponent n would be 0, as the bending friction factor is constant for turbulent flow. For laminar flow the exponent n is negative, but not smaller than -1. For n equals -1 there would be only wall friction like in straight laminar channel flow. The friction factor can be calculated in relation to the velocity or the Re number. Only the coefficient changes, the exponent stays the same. The main difference to Eq. (3) is the separation of the length L from the coefficient. For smaller Re numbers the pressure loss by wall friction is dominant and hence, the channel length has a big influence on the pressure loss. Eqs. (1) and (4) will be the approaches applied in this work.

5.1. Simulation of fluid dynamics

The volume-of-fluid program CFD-ACE + 2006 from ESI Group is used for all numerical simulations. The boundary conditions of the following simulations are all equal: Fully developed laminar velocity profile at the inlet and zero pressure at the outlet. The mesh size is 5 μm in all directions. The used fluid here is water. The shape of the particular simulated channel element has a large influence on the convergence behavior of the simulations. For static simulations, elements with 90° bends and joints did not converge for inlet Re numbers higher than 500, whereas the elements with radii or wedges converged for Re numbers even higher than 1000. The modifications of the elements reduce the pressure and velocity gradients inside the channel, which are the main cause of the converging problems for the simulations of the 90° elements. Transient flow behavior, like described by Dreher et al. [20] for T-shaped micromixers, can be another reason. Therefore, transient simulations of the 90° elements have been made. These simulations converged for Re numbers up to 600–700 but then the high gradients lead to non-converging results, as well.

Fig. 5 shows the pressure loss of a T-joint without and with a wedge. The dashed line represents the analytical pressure loss caused by wall friction in the channel element. The pressure loss for both shapes is bent upwards with increasing Re numbers. The portion of pressure loss caused by the redirection becomes more dominant at higher Re numbers, but the pressure loss caused by wall friction cannot be neglected. The wedge significantly lowers the pressure loss caused by the bend (38% at Re = 700). The

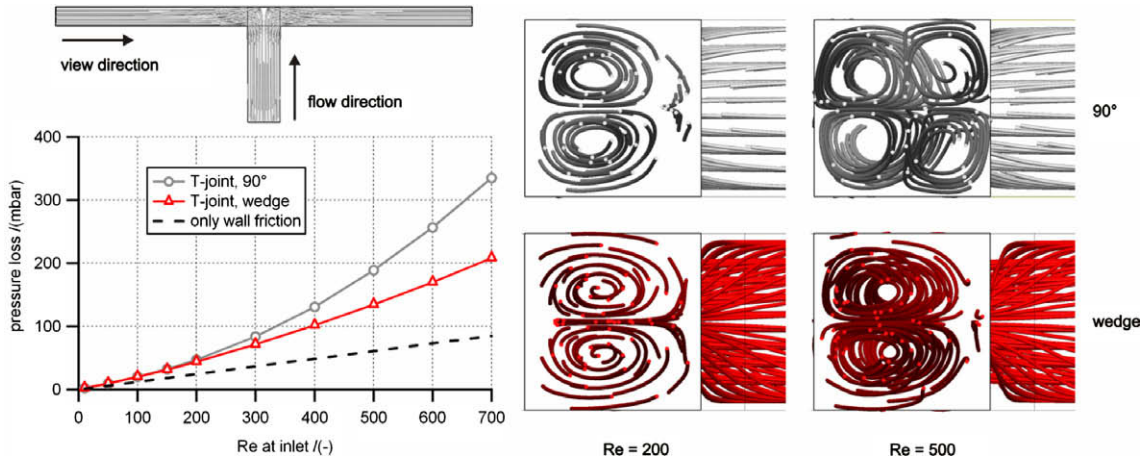

Fig. 5. Simulated pressure loss of T-joint and streamlines of the created vortices after the joint (90° on the top row, wedge on the bottom row; inlet Re number = 200 at the left column, inlet Re number = 500 at the right column).

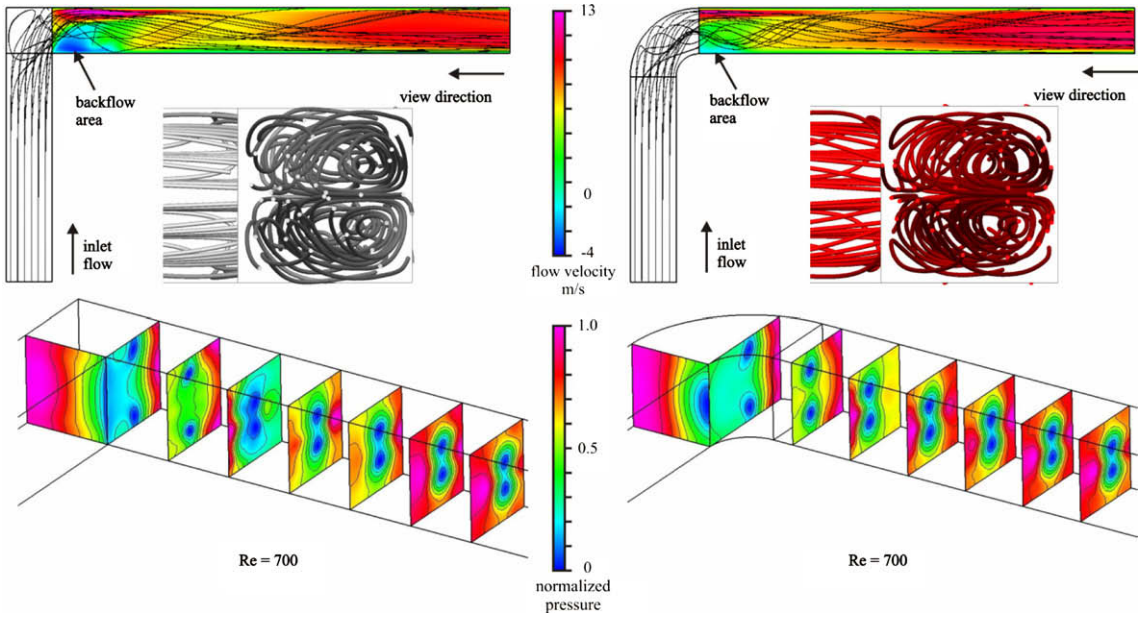

Fig. 6. Simulation results for both simulated L-bends at Re = 700; top: streamlines and flow velocity in direction of the outlet channel; bottom: normalized pressure for different cuts through the outlet channel which shows the movement of the center of the vortices.

reduction of pressure loss increases with the Re number. Depending on the Re number, the redirection of the fluid leads to vortices caused by the centrifugal force [3]. The centrifugal force increases linearly with the bending radius. The wedge decreases the bending radius and hence, the centrifugal force. The wedge also prevents the fluid from hitting the back wall with a flow direction perpendicular to the wall. The fluid is smoothly redirected, which also leads to weaker vortices. Fig. 5 shows the created vortices for both shapes for Re = 200 and Re = 500 at the inlet, looking from the outlet towards the joint. For inlet Re numbers smaller than 10, the bend does not disturb the laminar flow. For Re numbers smaller than 100 the flow is disturbed, but no entire vortices are created. For higher Re numbers a pair of vortices is created. At Re = 200 the 90° T-joint creates a pair of vortices that does not occupy the whole cross section. The center of the vortices is shifted towards the outer wall. The pair of vortices created by the T-joint with a wedge is weaker, but occupies almost the whole cross section. For increasing Re numbers the center of the vortices created by the 90° joint moves more and more toward the outer wall. Beginning at Re = 400, the first created pair of vortices of the 90° T-joint creates a second pair of vortices after the joint in the area close to the inner wall. This phenomenon has been described in several publications [21–22]. At Re = 500, shown in Fig. 5, the T-joint with the wedge still creates only one pair of vortices, the center of the vortices has only slightly moved toward the outer wall. At Re = 1000, the highest simulated inlet Re number for this element, the second pair of vortices started to emerge, but the vortices were not completely developed.

The simulation results of the L-bend show as well similarities as differences, compared to the T-joint. The L-bend with the 90° bend has a significantly higher pressure loss than the L-bend with a radius. For an inlet Re number of 700 the reduction in pressure loss is 33%. The vortices of the 90° L-bend are stronger than the respective vortices of the L-bend with radius, but in the examined range (up to Re = 700 for the 90° bend and up to Re = 1500 for the bend with the radius) only one pair of vortices is created for all shapes. Contrary to the T-joint, the center of the created pair of vortices does not stay at the outer wall of the outlet channel. Fig. 6 explains that behavior in more detail. In the lower part of Fig. 6 the normalized pressure at different cuts of the outlet channel is shown. In this case, normalized pressure means the pressure is normalized at each cut compared to the local maximum and minimum pressure of the particular cut. This enables an accurate view on the movement of the center of the vortices along the channel. In the center of the vortices the normalized pressure is zero. For both shapes, the center of the vortices travels from the outer wall to the inner wall and back to the outer wall on its way from the bend to the outlet. Even though the cross section of the channel is the same than the cross section of the outlet channel of the T-joint, there is no space for creating a second pair of vortices in case of the simulated L-bend. Nevertheless, the radius lowers the strength of the created vortices somewhat and, what is more relevant, reduces the backflow in the area next to the inner wall close to the bend (see upper part of Fig. 6). This backflow, also called transverse vortices, leads to hot spots near the inner corners [17]. The radius significantly reduces this backflow. At Re = 700 the maximum backflow velocity is reduced from 3.4 to 1.2 m s^{-1}.

The simulations of the fork-shaped elements show an equivalent behavior to the simulations of the single elements. For the 90° fork-shaped branch the static simulations converged up to Re = 400 and the transient simulations up to Re = 500. The pressure reduction for an inlet Re number of 500 is 28%. This is somewhat smaller than the reduction of pressure loss in the single elements, but it has to be considered, that the Re number at the L-bend of the fork-shaped element is lower than the entrance Re number. Like in the simulations of the T-joint, a second pair of vortices is created in the subsequent channel after a 90° T-joint for inlet Re numbers of 400 and higher. After the following L-bend, one pair of vortices is left.

Next, the introduced approaches for the pressure loss are applied to the simulations results. First, the approach with the bending friction factor, shown in Eq. (1), is tested. Rearranging of Eq. (1) and substituting the velocity by the Re number lead to:

$$\zeta_b = (\Delta p - \Delta p_{fr}) \frac{2\rho}{\eta^2} \frac{d_h^2}{Re^2} \tag{5}$$

The wall friction pressure loss p_{fr} is calculated analytically with the first term of Eq. (2), C_f is obtained from literature [2]. The results for the different calculated bending friction factors are shown in Fig. 7.

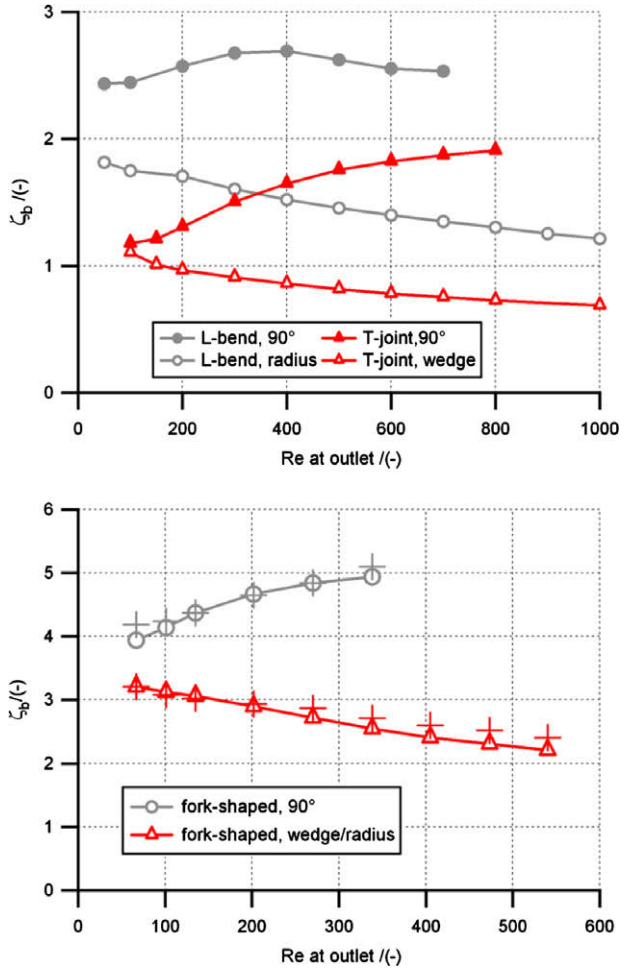

Fig. 7. Bending friction factor ζ_b for all simulated elements; top: single L-bend and T-joint; bottom: fork-shaped element.

The upper graph of Fig. 7 shows the calculated bending friction factor ζ_b for the single simulated elements. In case of the L-bend, ζ_b has a maximum at Re = 400 and is slightly decreasing for higher Re numbers. The calculation of the bending friction factor for the T-joint has to be treated differently. The diameter changes after the T-joint and therefore, the outlet Re number is smaller than the inlet Re number. The vortices occur in the outlet area and most of the channel length has the outlet diameter. Hence, the outlet Re number and the outlet diameter are used to determine ζ_b. The bending friction factor of the 90° T-joint is increasing. The main cause for that behavior is certainly the second pair of vortices that is created. It seems that this factor also has a maximum, but it did not reach that maximum in the examined range. The bending friction factor of the bend with radius and the joint with wedge look similar, only separated by a constant offset. Both factors are decreasing with the Re number. The factors seem to reach an asymptotic value. This is correct, as the factors are constant for turbulent flow. The bottom graph of Fig. 7 shows the bending friction factor calculated out of the simulations of the fork-shaped element. They are also related to the outlet Re number and diameter. The additional crosses show the sum of the bending friction factor of the single elements (ζ_b of the T-joint plus ζ_b of the L-bend). The differences between the values calculated from the simulations of the fork-shaped element and the values obtained by adding the two single factors are smaller than 5% at each Re number. Neglecting the smallest Re numbers, the differences become larger for higher Re numbers. The laminar flow profile was not able to completely recover after the T-joint before the L-bend was reached. The simulations of the single elements forced the outlet pressure to be zero, which probably caused these little discrepancies. Nevertheless, the presented results show that the bending friction factor of a complex element can be approximated if the factors of the single elements for the specific Re numbers are known.

Table 2
Data for regression fit of pressure loss for simulated elements.

Shape	P_{max} (mbar)	Re_{max} (in/out)	m^*	n	R^2
L bend 90	280	400/400	14.98	−0.66	0.990
L bend radius	210	400/400	23.67	−0.78	0.998
T-joint 90	131	500/340	10.85	−0.60	0.983
T-joint wedge	102	500/340	10.85	−0.60	0.983
Fork 90	247	400/270	31.63	−0.70	0.984
Fork W/R	190	500/340	48.12	−0.80	0.997

Table 2 presents the results of the regression fit of Eq. (4) applied on the pressure loss of the simulations. The fit function is related to the Re number at the inlet. Whether the inlet or outlet Re number is applied does not influence the result for the exponent n. The applied Re number only changes the coefficient m by a constant factor that is determined by the ratio between inlet and outlet diameter and the exponent n. These data show some similarities between the elements with similar shapes. The geometries with sharp 90° bends and joints have an exponent n between −0.60 and −0.70. The elements with the radii or wedges have an exponent between −0.78 and −0.82. The coefficient m is smaller for geometries with a higher pressure loss. This compensates the larger exponents at lower Re numbers, where the pressure loss of the different shapes is similar. The coefficients of the fork-shaped elements are approximately the sum of the coefficients of the single elements, which mirrors the tendency of the bending friction factor of Fig. 7. The regression fit of the 90° bends and joints is worse than the regression fits of the geometries with wedges and radii.

5.2. Experimental determination of pressure loss

In the experiment it was possible to examine much higher Re numbers than in the simulations. On the other hand the investigation of low Re numbers is very difficult, as the mass flow rates and the pressure losses are very small and therefore, very difficult to measure. With a maximum flow rate of 4.2 l/h the resulting maximum Re number is 3000 for the fabricated inlet channels. In textbooks [23], the critical Re number that indicates the transition from laminar to turbulent flow is given as 2300. It has to be considered, that the Re number in the fork-shaped devices FT is reduced at each T-joint. The fabricated devices have three branching levels, see Fig. 2, which means an inlet Re number of 3000 is reduced to 2100 at the first T-joint, to 1300 at the second T-joint, and to 750 at the third T-joint. The flow changes from turbulent at the inlet to laminar at the outlet.

Like in the simulations, the graphs of the experimental pressure loss are bent upwards. Due to entrance effects, the straight channel SC also does not have a linear increasing pressure loss. These entrance effects can be approximated by taking the difference between analytical wall friction and experimental pressure loss of the straight channel. The same entrance effects occur at the devices L-90 and L-WR, but if they are known from the straight channel SC, they can be excluded from the results. Compared to the device L-90, the device L-WR with the radius has a lower pressure loss between 25% and 28%, depending on the Re number. The upper graph of Fig. 8 shows the reduction of pressure loss between the different shapes of the devices FT. The absolute pressure loss reduction of the pressure optimized versions compared to the heat transfer

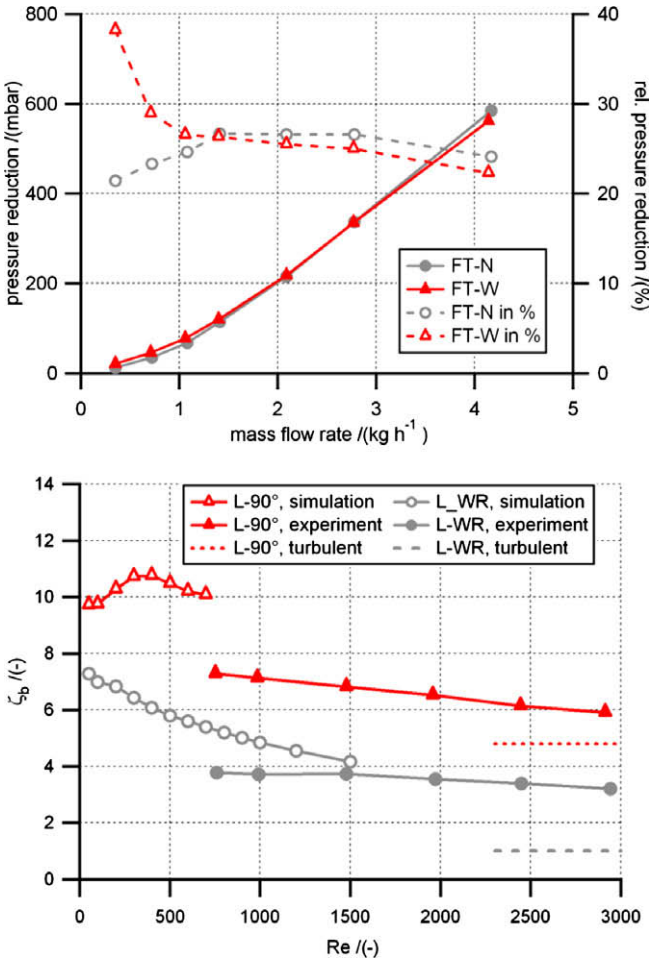

Fig. 8. Experimental results of pressure loss, top: pressure reduction for fork-shaped devices FT; bottom: bending friction factor for L-90 and L-WR compared to simulation results.

optimized versions is increasing with the Re number and does not depend on the overall width of the branches. The relative pressure loss reduction is nearly constant for an inlet Re number between 1000 and 2000. For lower inlet Re numbers the respective Re numbers after the branchings are even smaller. An inlet Re number of 500 leads to an outlet Re number of 125. For such low Re numbers the different shapes influence the pressure loss very little and the overall pressure losses are very small. At higher mass flow rates the flow becomes turbulent for some parts of the device and the pressure reduction is somewhat reduced.

The bottom graph of Fig. 8 shows the calculated bending friction factor ζ_b of the experiments according to Eq. (5) and compares it with the simulation results. The results of the simulations are obtained by taking four times the bending friction factor of one bend, as the fabricated device has four L-bends. The values for turbulent flow (taken from [24]), that are also included in the graph, are valid for circular cross sections with arbitrary hydraulic diameter, but they show the order of magnitude of the bending friction factors for turbulent flow. The factor slightly decreases for both shapes and even for Re = 3000 it has not reached its asymptotic value. The simulation results are higher than the experimental results and are more dependent on the Re number, especially the results of the 90° L-bend. For higher Re numbers the differences between the simulated and the measured L-bend with radius become smaller. The tendency of the simulated 90° bend indicates the same behavior. One possible reason for the lower experimental bending

Table 3
Data for regression fit of pressure loss for experimental results.

Shape	P_{max} (mbar)	Re_{max} (in/out)	m^*	n	R^2
Four bends 90	1663	2470/2470	3.97	−0.39	1.000
Four bends radius	1123	2470/2470	6.46	−0.52	0.998
FT-W-90	1340	2000/501	4.10	−0.39	1.000
FT-W-WR	1005	2000/501	3.69	−0.42	1.000
FT-N-90	1268	2007/502	3.71	−0.37	0.998
FT-N-WR	931	2007/502	3.28	−0.40	1.000

friction factor is the different aspect ratios of channel geometries of simulation and experiment. The approximation of the entrance effects can also cause some inaccuracies.

Table 3 shows the data obtained by applying the regression fit introduced in Eq. (4) to the experimental results. Re numbers higher than 2500 have not been included into the data fit, as this would be turbulent flow. Again, the shapes with the 90° bends and joints have similar exponents of 0.37–0.39. The exponents of the pressure optimized fork-shaped test structures FT do also match, only the four bends with a radius have a deviant value. The mathematical fit matches the experimental values very well, but only if Re numbers smaller than 500 are neglected. For lower inlet Re numbers the wall friction is more dominant, for higher Re numbers the pressure loss caused by the bends and joints is more dominant. The used fitting function is not able to cover both ranges. A more suitable model for both ranges is given in the following equation:

$$F^* = \frac{c}{\mathrm{Re}} + m^* \cdot \mathrm{Re}^n \tag{6}$$

Like the very first approach in this work, this approach distinguishes between pressure loss caused by wall friction or by redirection of the fluid. For n equals 0 this approach becomes the very first approach of this work with a constant bending friction factor ζ_b. This factor has appeared not to be constant for bent, laminar flow, so the approach in Eq. (6) seems to be more accurate. Unfortunately, this approach is very difficult to apply to elements with different Re numbers and diameters, as used in this work.

The experimental results do not match the results of the simulations. The simulations have exponents in the range of 0.65–0.70 (90°) and 0.78–0.82 (wedge/radius). The simulations only examined Re numbers up to 500, which had to be neglected for the experimental results. This shows that the range between Re = 10 and Re = 2000 cannot be treated as one continuous range. Several physical phenomena like creation of one or two pair of vortices start to develop in the examined range, which influences the fluid flow behavior. More experiments and more simulations with different aspect ratios are necessary in order to collect more information. More experimental data, especially at lower Re numbers, have to be collected and compared to the simulation results. Out of this information the pressure loss within the different ranges of Re numbers can be approximated more precisely and more accurate statements can be made. The transition between the different ranges also depends on the shape of the bends and junctions. This phenomenon also has to be examined in more detail.

6. Heat transfer and effectiveness

6.1. Simulation of heat transfer

The absorbed heat can be determined from the temperature increase of the heated fluid:

$$\dot{Q} = \dot{m} \cdot c_p \cdot (T_{m,out} - T_{m,in}) \tag{7}$$

The absorbed heat can be used for calculating a mean heat transfer coefficient:

$$h = \frac{\dot{Q}}{A_{\text{channel}} \cdot \Delta T_{\log}} = \frac{\dot{m} \cdot c_p \cdot (T_{\text{m,out}} - T_{\text{m,in}})}{A_{\text{channel}} \cdot \Delta T_{\log}} \tag{8}$$

The logarithmic temperature gradient is defined as following:

$$\Delta T_{\log} = \frac{\Delta T_{\text{out}} - \Delta T_{\text{in}}}{\ln(\Delta T_{\text{out}} / \Delta T_{\text{in}})} \tag{9}$$

The temperature differences are defined as $\Delta T_{\text{out}} = T_W - T_{\text{m,out}}$ and $\Delta T_{\text{in}} = T_W - T_{\text{m,in}}$. In all simulations of this work the wall temperature is kept constant at 350 K. Only the top wall of the channel is defined as adiabatic in order to simulate the Pyrex cover of the fabricated devices. The fluid inlet temperature is 300 K. First, the simulations are calculated with constant properties in order to keep the evaluations more simple. Later, the simulations have been repeated with temperature depending properties. With the applied boundary conditions the flow that enters the channel is hydrodynamically developed, but not thermally. The developing thermal profile has a cold center flow and an increasing fluid temperature towards the wall. The temperature gradient at the wall is decreasing in flow direction. Redirecting and splitting the flow disturbs that thermal profile. The cold center flow is pushed against the back wall and the created vortices mix the colder sections of the fluid with the warmer sections. The temperature gradient at the wall and hence, the heat transfer rate, is significantly increased. Fig. 9 shows the local Nu number of a T-joint followed by an L-bend.

The definition of the local Nu number is given in Eq. (10). It can be determined from the local heat flow rate and the local temperatures.

$$Nu_{\text{loc}} = \frac{h_{\text{loc}} \cdot d_h}{k} = \frac{\dot{q}_{\text{loc}} \cdot d_h}{k \cdot (T_{\text{w}} - T_{\text{m,loc}})} \tag{10}$$

For a thermally and hydrodynamically developed flow the Nu number is constant (4.12 at a squared cross section with constant wall temperature). The fluid that enters the channel is thermally not developed and therefore, the Nu number is higher at the entrance. Along the channel the Nu number decreases and reaches its asymptotic value of a straight channel. In the simulated element a T-joint splits the fluid after 500 μm. The local Nu number is increased, depending on the shape of the T-joint. After the joint the Nu number is decreasing, again, but slower than after the inlet. This is the result of the created vortices. The Nu number of the 90° T-joint is higher than the Nu number of the T-joint with a wedge, at the joint itself and in the channel behind the joint. The wedge reduces the pressure loss which leads to weaker vortices and therefore, the heat transfer is smaller. The following L-bend increases the Nu number again. This time, the shape of the bend only influences the Nu number at the bend itself. In the area of the bend the Nu number of the 90° bend is higher than the Nu number of the bend with radius, but behind the bend the two Nu numbers are equal. The fluid that arrives at the L-bend is already heated and has no typical thermal profile with a cold center flow. Differences in the strength of the vortices are not as decisive as after the T-joint.

The properties of water depend on the temperature, especially the viscosity. A higher fluid temperature leads to a slightly higher thermal conductivity and to a lower viscosity. The simulations with variable properties show a similar behavior as the simulations with constant properties, but the heat transfer is enhanced. The pressure loss is reduced for variable properties. The reduction of pressure loss decreases with the flow rate, as the mean fluid outlet temperature decreases. At Re = 400 at the inlet, the mean outlet fluid temperature is 324.0 K (90°) and 321.6 K (WR). This leads to a 27% (90°) and 33% (WR) lower pressure loss of the simulations with variable properties compared to constant properties.

In Fig. 10 the simulation results of the heat transfer are shown. The upper graph summarizes the mean heat transfer coefficients of all simulated elements. All elements with wedge or radii have very similar heat transfer coefficients and all elements with 90° bends or joints have very similar heat transfer coefficients. Only for higher Re numbers the L-bend shows little smaller coefficients. The 90° elements definitely have a higher mean heat transfer coefficient than the respective elements with a radius or a wedge. With higher Re numbers the differences become larger, only for Re numbers smaller than 100 the coefficients are similar. At such small Re numbers there are no or only little vortices created at the bends and the influence of the shape is negligible.

6.2. Effectiveness of simulated geometries

The shapes with the lower pressure loss do also have a lower heat transfer coefficient. That means for the same mass flow rate the elements with the 90° bends and joints absorb more heat. In order to compare the real effectiveness of the different shapes of bends and joints, the absorbed heat and the pressure loss have to be considered at the same time. For the evaluation of the effectiveness it is more reasonable to use the pumping power, introduced in Eq. (11), instead of the pressure loss.

$$\dot{W} = \frac{\dot{m} \cdot \Delta p}{\rho} \tag{11}$$

The bottom graph of Fig. 10 shows the effectiveness of the simulated elements. For an L-bend the effectiveness of the two different shapes is similar. The lower pressure loss of the bend with the radius compensates the lower heat transfer coefficient. This is not the case for the T-joint, where the lower pressure loss of the joint with the wedge cannot compensate the full disadvantage of the lower heat transfer coefficient. The effectiveness of the 90° joint is

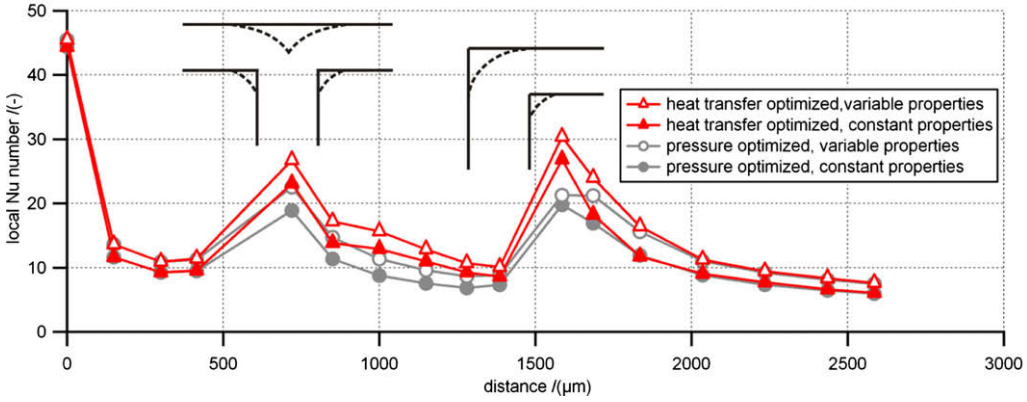

Fig. 9. Local Nu number for a fork-shaped element at Re_{in} = 400 for constant and variable properties.

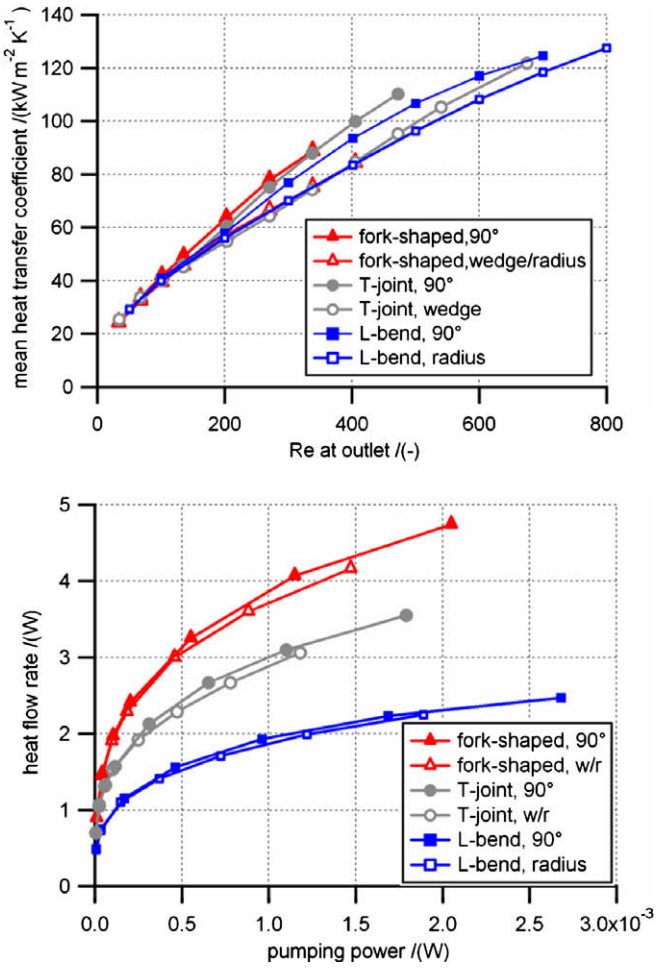

Fig. 10. Simulation results of heat transfer; top: mean heat transfer coefficients, bottom: effectiveness for Re numbers up to 600 (L-bend and T-joint) and 500 (fork-shaped).

higher than the effectiveness of the joint with the wedge. The effectiveness of the combined element shows the same behavior. The differences in the effectiveness are not very large, but they are not negligible. For larger Re numbers or mass flow rates the differences will become more significant.

6.3. Heat transfer in experiment

As depicted in Fig. 4, the fabricated chips are tested with different temperatures of the hotplate. The temperature of the hotplate T_H is not the temperature at the bottom of the chips. The temperature decreases towards the chip due to the thermal resistance of the brass block and several contact resistances, estimated in Section 4. The measured chip temperature has to be treated with caution. The temperature across the chip is not constant and the five Pt100-sensors only give an approximation of the local temperature. The positions of these five sensors influence the results. More sensors would deliver a more accurate chip temperature.

Calculating a mean heat transfer coefficient for a fabricated device is much more difficult as it has been for the simulations. The wall temperature is not constant and unknown. These limitations lead to the definition of the thermal resistance of the chip:

$$R_{th} = \frac{(\overline{T}_{chip} - \overline{T}_{fluid})}{\dot{Q}} \qquad h_{exp} = \frac{1}{R_{th} \cdot A_{channel}} \tag{12}$$

In this definition the mean chip temperature is used instead of the wall temperature. The mean fluid temperature is the mean value of inlet and outlet fluid temperature. The resulting heat transfer coefficient h_{exp} is the reciprocal value of the thermal resistance times the channel surface area. The upper graph of Fig. 11 shows the mean heat transfer coefficient h_{exp} (continuous line) and the mean measured chip temperature (dashed line) for the devices L-90 and SC for heating temperatures of 60 and 80 °C. At equal heating temperatures the bent channel L-90 has a lower chip temperature than the straight channel SC. With increasing mass flow rates the chip temperatures are decreasing. The experimental mean heat transfer coefficient h_{exp} of the bent channel L-90 is distinctly higher than the coefficient of the straight channel SC. Assuming constant material properties, the heat transfer coefficient should not depend on the heating temperature. In the presented results, in case of the straight channel the heat transfer coefficient for T_H = 60 °C is higher than the respective coefficient for T_H = 80 °C. In case of the four times bent channel it is the other way round. Throughout the experiments with different heating temperatures the cooling chips have not been removed and hence, the contact resistances should not have changed. The calculated heat transfer coefficients depend on three measured temperatures, the fluid inlet and outlet temperature, and the mean chip temperature. Small inaccuracies in the measured data can sum up and lead to the obtained deviation.

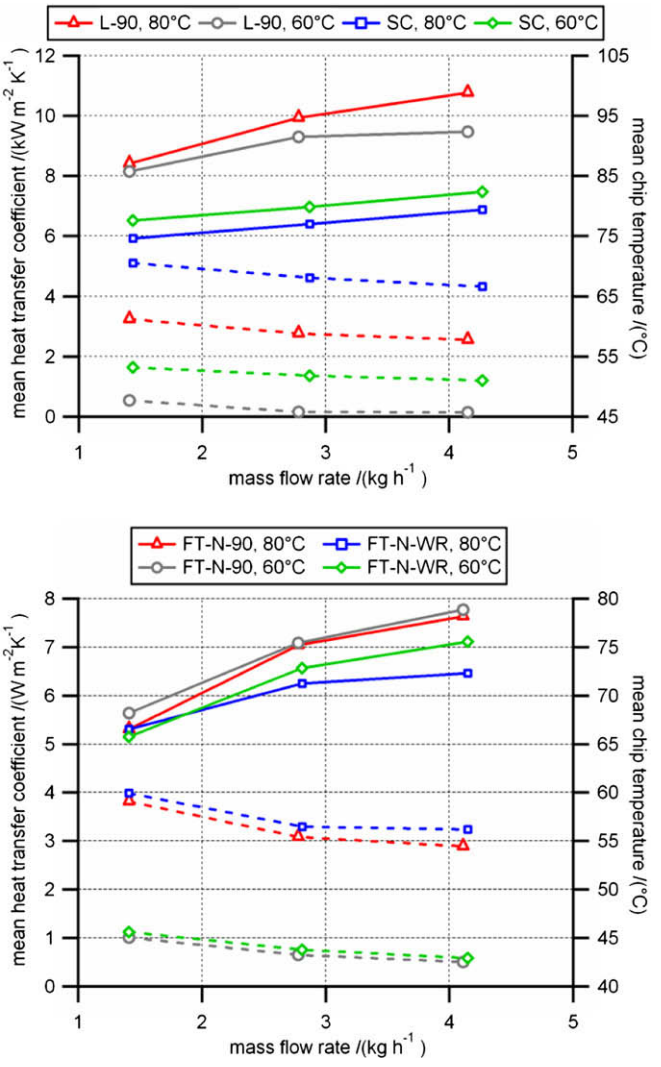

Fig. 11. Experimental heat transfer coefficient (continuous line) and mean chip temperature (dashed line); top: SC and L-90; bottom: FT-N-90 and FT-N-WR.

The small resolution in measuring the chip temperature distribution is probably the main cause for the deviation. However, the higher heat transfer coefficient of the bent channel is clearly visible. It is difficult to compare the simulated heat transfer coefficients with the experimental values. The experimental heat transfer coefficients h_{exp} are in the range of 8–12 kW m^{-2} K^{-1}, the simulated coefficients h are in the range of 60–125 kW m^{-2} K^{-1} at the highest simulated Re numbers. The simulated and the experimental heat transfer coefficients do not match, due to the differences between the boundary conditions in the simulations and the real conditions of the experimental setup. The simulated values are calculated with regards to a constant wall temperature. This is not the case in the experiments, where the mean measured bottom chip temperature is used to determine the mean heat transfer coefficient. The measured chip temperature is not constant and higher than the actual wall temperature. A lower temperature in Eq. (12) would lead to a lower thermal resistance and a higher heat transfer coefficient h_{exp}.

The bottom graph of Fig. 11 shows the calculated thermal heat transfer coefficient h_{exp} of the two different narrow branches FT-N-90 and FT-N-WR, and the respective mean chip temperatures. Again, the heat transfer coefficients show a very small variation for different heating temperatures. The reasons will be the same as explained above. The heat transfer coefficients of FT-N-90 are higher than the coefficients of FT-N-WR. The differences between the heat transfer coefficients increase slightly with the mass flow rate. The mean chip temperatures decrease with the mass flow rate and are significantly lower than the heating temperatures. At T_H = 60 °C the chip temperatures of FT-N-90 and FT-N-WR are similar, at T_H = 80 °C the chip temperature of FT-N-90 is lower. The variances in the local chip temperature can reach up to 6 K at T_H = 60 °C and 8 K at T_H = 80 °C. This fact corroborates the need for a higher resolution in measuring the local chip temperatures. Having only five temperature sensors for such high temperature variances across the chip will unavoidably lead to inaccuracies, especially in the calculated mean chip temperature. A higher resolution would provide a more detailed analysis and probably decrease the difference in heat transfer coefficients for different heating temperatures.

6.4. Experimental effectiveness

The left hand side graph of Fig. 12 shows the effectiveness of the straight channel SC compared to the bent channel L-90 for a hotplate temperature T_H of 40, 60 and 80 °C. The calculated Re numbers of the applied mass flow rates are 1040, 2072, and 3082. Despite the much higher pressure loss and, hence, a higher needed pumping power, the effectiveness of the bent channel is much higher. With an increasing heating temperature or increasing mass flow rate the advantage of the bent channel becomes larger. Even for much higher pumping powers as examined, the straight channel SC will never absorb as much heat as the bent channel did for comparable small pumping powers. For the same amount of applied pumping power the bent channel will always absorb more heat than the straight channel. Therefore, the bent channel always has the higher effectiveness.

The fork-shaped test structures are tested at T_H = 60 °C and T_H = 80 °C, as shown in the right hand side graph of Fig. 12. Compared to the simulation results, the heat transfer optimized structures (FT-W-90 and FT-N-90) show a more significant higher effectiveness than the pressure optimized structures (FT-W-WR and FT-N-WR). For T_H = 60 °C and the lowest measured mass flow rate of 1.4 kg h^{-1}, which corresponds to an inlet Re number of 1000 and a Re number at the outlet of the branch of 255, the differences are very small. This matches with the conclusions of the simulations with only very little differences in the effectiveness for Re numbers up to 600. At higher heating temperatures or higher mass flow rates the differences become larger. Due to the longer overall channel length the wider branch FT-W absorbs more heat than the narrow branch FT-N. The rise in heat transfer is larger than the rise in pressure loss, which leads to a higher effectiveness of the wider branch. This enhancement is also increasing with the heating temperature and the mass flow rate. The most important conclusions from this graph is the fact that each reduction in pressure loss by changing the shape of the bend or joint always leads to a lower effectiveness.

7. Conclusion

The aim of this work is to investigate the pressure loss and the heat transfer coefficients of microchannels with bends and junctions on the basis of simple elements like L-bends and T-joints, and the combination of the two elements, the fork-shaped element. The numerical and experimental results show the enhancement in heat transfer that can be achieved by redirecting and splitting the fluid. Due to the vortices in curved flow, the temperature gradient is increased at the wall, which leads to an enhanced heat transfer. The cost for such an enhanced heat transfer is a higher pressure loss, demanding a higher pumping power. The effort can be reduced by changing the geometry of the bends and joints, but at the same time the heat transfer is reduced as well. The evaluation of the effectiveness has shown that a lower pressure loss always leads to a lower effectiveness. The shapes with the highest pressure losses have the highest effectiveness. The advantages of the heat transfer optimized elements become larger at higher chip temperatures and higher

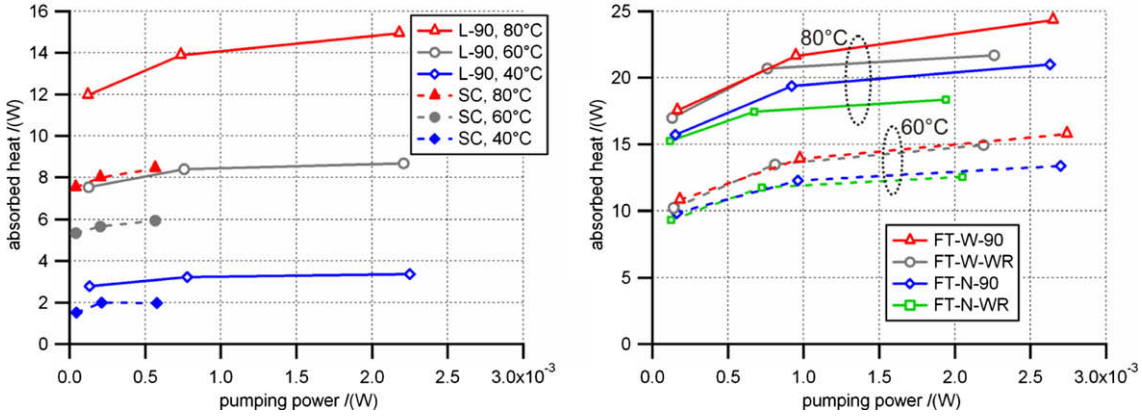

Fig. 12. Effectiveness of test structures; left: L-90 and SC at T_H = 40 °C, 60 °C, and 80 °C; right: FT-W and FT-N at T_H = 60 °C (dashed line) and T_H = 80 °C (continuous line).

mass flow rates. The presented work provides the fundamentals to build a complete cooling device based on elemental structures. Branches, like shown in this work, can be combined according to Bejan's "Constructal method" to build a fluidic cooling device with a very high heat transfer coefficient.

The attempt to find a mathematical model that approximates the pressure loss of the disturbed laminar flow with vortices in bent microchannels contains some obstacles. Depending on the Re number, no vortices, one pair, or two pairs of vortices are created. Laminar and turbulent flow aspects influence the pressure loss. Shape and aspect ratios do also have a very large influence on pressure loss. The presented approaches in this work enable a rough approximation of the pressure losses in channel networks and a comparison between different shapes. The method with the bending friction factor can be used for calculating the pressure loss of more complex structures, but more experimental evaluations of different simple shapes and aspect ratios are still necessary.

References

[1] S.G. Kandlikar, High flux heat removal with microchannels – a roadmap of challenges and opportunities, in: International Conference on Microchannels and Minichannels, 2005, 75086.
[2] M. Gad-el-Hak (Ed.), The MEMS Handbook, CRC Press, Boca Raton, FL, 2001 (Chapters 4 and 6).
[3] N. Kockmann, M. Engler, D. Haller, P. Woias, Fluid dynamics and transfer processes in bended microchannels, Heat Transfer Eng. 26 (2005) 71–78.
[4] N. Kockmann, T. Kiefer, M. Engler, P. Woias, Convective mixing and chemical reactions in microchannels with high flow rates, Sensors Actuators B 117 (2006) 495–508.
[5] N. Kockmann, T. Kiefer, M. Engler, P. Woias, Channel networks for optimal heat transfer and high throughoutput mixers, in: International Conference on Heat Transfer and Fluid Flow in Microscale, 2005.
[6] N. Kockmann, D. Haller, P. Woias, Optimierte Mikro-Kühlkanäle für thermisch hochbelastete Bauteile, Chem. Ing. Tech. 78 (2006) 1202–1203.
[7] N.R. Rosaguti, D.F. Fletcher, B.S. Haynes, Laminar flow in a periodic serpentine channel, in: Proceedings of the 15th Australien Fluid Mechanics Conference, 2004.
[8] N.R. Rosaguti, D.F. Fletcher, B.S. Haynes, Low-Reynolds number heat transfer enhancement in sinusoidal channels, Chem. Eng. Sci. 62 (2007) 694–702.
[9] I. Papautsky, B.K. Gale, S. Mohanty, T.A. Ameel, A.B. Frazier, Effects of rectangular microchannel aspect ratio on laminar friction constant, in: C.H. Ahn, A.B. Frazier, (Eds.), Proceedings of SPIE, Microfluidic Devices and Systems II; vol. 3877, 1999, pp 147–158.
[10] A. Bejan, Constructal-theory network of conducting paths for cooling a heat generating volume, Int. J. Heat Mass Transfer 40 (1996) 799–816.
[11] A. Bejan, Shape and Structure, From Engineering to Nature, Camebridge University Press, Camebridge, 2000.
[12] D.R. Emerson, K. Cieslicki, X. Gu, R.B. Barber, Biomimetic design of microfluidics manifolds based on a generalized Murray's law, Lab on a Chip 6 (2006) 447–454.
[13] V.D. Zimparov, A.K. da Silva, A. Bejan, Constructal tree-shaped parallel flow heat exchangers, Int. J. Heat Mass Transfer 49 (2006) 4558–4566.
[14] Y. Chen, P. Cheng, Heat transfer and pressure drop in fractal tree-like microchannel nets, Int. J. Heat Mass Transfer 45 (2002) 2643–2648.
[15] Y. Chen, P. Cheng, An experimental investigation on the thermal efficiency of fractal tree-like microchannel nets, Int. J. Heat Mass Transfer 32 (2005) 931–938.
[16] D.V. Pence, Reduced pumping power and wall temperature in microchannel heat sinks with fractal-like branching channel network, Microscale Thermophys. Eng. 6 (2002) 319–330.
[17] S.M. Senn, D. Poulikakos, Laminar mixing, heat transfer and pressure drop in tree-like microchannel nets and their application for thermal management in polymer electrolyte fuel cells, J. Power Sources 130 (2004) 178–191.
[18] E.W. Zerbst, Bionik, Biologische Funktionsprinzipien und ihre technischen Anwendungen, Teubner Studienbücher, 1987.
[19] E. Truckenbrodt, Fluidmechanik, Springer, Heidelberg, 1996.
[20] S. Dreher, N. Kockmann, P. Woias, Characterization of laminar transient flow regimes and mixing in T-shaped micromixers, Heat Transfer Eng. 30 (2009) 91–100.
[21] L. Wang, T. Yang, Multiplicity and stability of convection in curved ducts: review and progress, Adv. Heat Transfer 8 (2004) 204–255.
[22] M.P. Arnal, Investigation of developing laminar and turbulent flow in curved ducts, Ph.D. Thesis, University of California, Bekeley, 1988.
[23] H. Oertel Jr., Prandtl-Führer durch die Strömungslehre, Vieweg Verlag, 2002.
[24] W. Bierwerth, Tabellenbuch Chemietechnik, Europa Lehrmittel, 2001.